# Semi-Analytical Magnetic Field Calculation for Dual-Rotor Permanent-Magnet Synchronous Machines by using Hybrid Model

Brahim Ladghem-Chikouche[1,2], Kamel Boughrara[2], Frédéric Dubas[3], Lazhar Roubache[1], and Rachid Ibtiouen[2]

[1]Department of Electrical Engineering, Faculty of Technology, University of M'sila, PB. 166, M'sila 28000, Algeria
[2]Département d'Electrotechnique, Laboratoire de Recherche en Electrotechnique (LRE-ENP), Ecole Nationale Polytechnique, rue des frères Oudek, Hacen Badi, BP. 182, El-Harrach 16200 Algiers, Algeria
[3]Département ENERGIE, FEMTO-ST, CNRS, Univ. Bourgogne Franche-Comté, F90000 Belfort, France

**Based exclusively on the exact subdomain (SD) technique and finite-difference method (FDM), this paper proposes a two-dimensional (2-D) hybrid model (HAM) for the semi-analytical magnetic field calculation in electrical machines at no-/on-load conditions. It is applied to dual-rotor permanent-magnet (PM) synchronous machines. The magnetic field is computed by solving Laplace's and Poisson's equations through exact SD technique in all regions at unitary relative permeability (i.e., PMs, air-gap and slots) with a numerical model based on FDM in ferromagnetic regions (i.e., teeth and rotor/stator yokes). These two models are specifically coupled in both directions (i.e., $r$- and $\theta$-edges) of the (non-)periodicity direction (i.e., in the interface between teeth regions and all its adjacent regions as slots and/or air-gap). To provide accurate solutions, the current density distribution in slots regions is modeled by using Maxwell's equations. Finite-element analysis (FEA) demonstrates highly accurate results of the developed technique. The 2-D HAM is ≈ 6 times faster than 2-D FEA.**

*Index Terms*—**Exact subdomain technique, finite-difference method, finite-element analysis, finite relative permeability, magnetic field, electrical machines.**

## I. INTRODUCTION

THE growing interest in the various modeling techniques used for the design of electrical machine has become a challenge to numerical approaches. However, these techniques remain limited by several assumptions such as the nonlinearity of the *B(H)* curve which gives overestimation and inaccuracy information on the magnetic field distribution especially in partial overlapping regions such as stator teeth and tooth-tips in which magnetic saturation effect is not negligible.

### A. A Review of the Existing Different Approaches

The solution of a system of partial differential equations (PDEs) resulting from Maxwell's equations applied to electrical machines can be performed by different methods, viz.,

i) numerical methods (e.g., FEA, FDM, …);

ii) the magnetic equivalent circuit (MEC), i.e., reluctance or permeance network, which are inappropriate and tedious for iterative design process;

iii) Maxwell-Fourier methods [1]-[15] (i.e., multi-layers models, eigenvalues model, harmonic modeling, no-exact/exact/elementary SD technique);

iv) Schwarz-Christoffel mapping method [16]-[18];

v) Hybrid method combining between:
- Conformal mapping and MEC [19]-[21];
- FEA and MEC [22]-[23];
- Maxwell-Fourier methods and FEA [24]-[25];
- Maxwell-Fourier methods and MEC [26]-[33];
- FDM and FEA [34]-[37];
- FDM and analytical model [38]-[39].

An example for a comparative analysis of various methods has been made in [40]-[41].

In [2]-[3], Dubas and Boughrara improve the SD technique in Cartesian and polar coordinates by taking into account the finite relative permeability of iron parts. This exact SD technique, using the principle of superposition in both directions (e.g., $x$- and $y$-edges in Cartesian coordinates [2] or $r$- and $\theta$-edges in polar coordinates [3]), allows for any non-periodic SD. This principle has been applied to various electromagnetic devices with excellent results, most recently on flat PM linear machines [14]. In [5]-[6], the authors extended the proposed model in [3] and [4] to elementary subdomains (E-SDs) in the rotor and/or stator regions with(out) electrical conductivities for the complete prediction of the magnetic field in electrical machines with the local saturation effect solved by the Newton-Raphson iterative algorithm. However, the exact SD and E-SD technique by inserting ferromagnetic regions is inappropriate for the reduction of the computational time.

The FDM is the most direct approach to discretizing PDEs. It is commonly used for various simulations because of its easy and flexible application on the computer. This method proceeds by discretizing the domain into a set of grid nodes. However, accuracy of results must be well controlled by means of an adequate number of grid nodes, an operation that is known to be more time consuming.

### B. Objectives of the Paper

In this paper, a novel 2-D HAM involving Maxwell-Fourier method, based on the exact SD technique, and FDM is proposed. It is applied to dual-rotor PM synchronous machines to consider the local or global saturation effect on electromagnetic performances whatever the relative permeability of iron parts as well as the load conditions. The proposed HAM can also improve the computational time and save the central processing unit memory. The exact SD technique is performed in all regions at unitary relative permeability (i.e., PMs, air-gap and slots). The FDM, which

**DOI**: 10.1109/TMAG.2021.3127359, IEEE TRANSACTIONS ON MAGNETICS

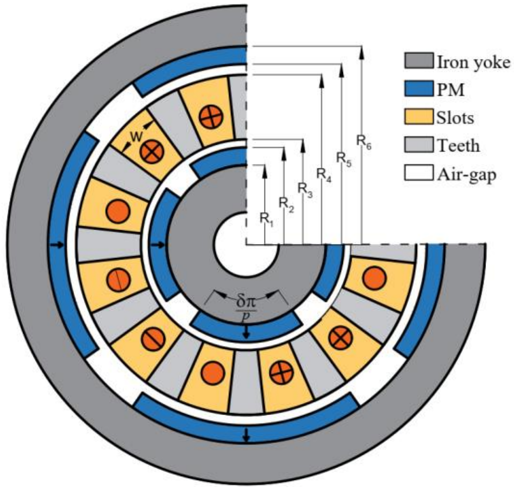


Fig. 1. Dual-rotor PM synchronous machine having a radial magnetization and a single-layer concentrated winding.

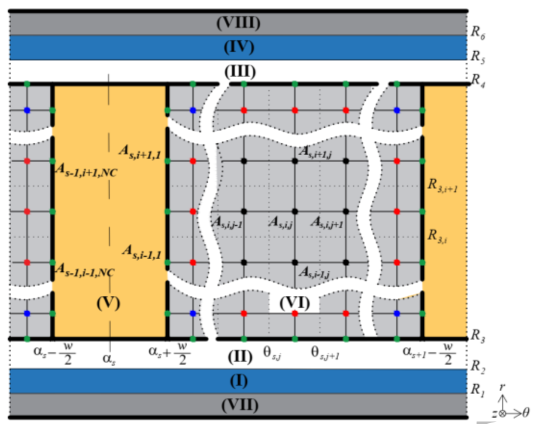


Fig. 2. Uniform mesh of the Region VI discretized into several nodes.

uses a nodal-mesh formulation, is implemented in ferromagnetic regions (i.e., teeth and rotor/stator yokes). The magnetic vector potential formulation has been used for both methods. The coupling between these models, which has not yet been realized in the literature, is performed in both directions (i.e., $r$- and $\theta$-edges). To evaluate the efficacy of the proposed HAM, the magnetic flux density distribution as well as the electromagnetic performances have been compared with those obtained by the 2-D FEA [42]. FEA demonstrates highly accurate results of the developed technique. The 2-D HAM is ≈ 6 times faster than 2-D FEA with high accuracy.

## II. Assumptions of the Model

The dual-rotor PM synchronous machine, indicated in Fig. 1, is constituted to some orthogonal subdomains. The subdomains I to VIII, shown in Fig. 2, are respectively: inner PMs, inner and outer air-gap, outer PMs, slots and teeth, inner and outer iron yoke.

The rotor topology is constituted of multi-pole PMs mounted on the rotor surface with a radial magnetization. Slots with radial sides surface is proposed in this work. The spatial distribution of *3*-phases winding is configurated in a standard manner with a single-layer in the slot (i.e., non-overlapping or concentrated winding).

In this paper, the proposed machine is described in a 2-D polar coordinate system. The magnetic field solution can be obtained under the same assumptions proposed in [14].

Usually, the results obtained in the slotless rotor core, as presented in the proposed machine, can be achieved easily and without difficulty. For this case, it is important to focused the proposed HAM for the regions where the slotting effect is presented, such as stator core. In this paper, it can be assumed that the rotor core has a fixed relative permeability and only the relative permeability of the stator part can be modified.

## III. Formulation of HAM

### A. Introduction

In this work, a 2-D HAM based exclusively on the SD technique and FDM is presented. Each SD of the proposed machine is modeled under constant absolute permeability and expressed by a PDE in terms of $\boldsymbol{A}$:

$$\nabla^2 \boldsymbol{A} = -[\mu \boldsymbol{J} + \mu_0 \nabla \times \boldsymbol{Mr}] \tag{1}$$

where $\boldsymbol{J}$ is the current density (due to supply currents) vector, $\boldsymbol{Mr}$ is the remanent magnetization vector (with $\boldsymbol{Mr} = 0$ for the vacuum/iron or $\boldsymbol{Mr} \neq 0$ for the PMs according to the magnetization direction), and $\mu = \mu_0 \mu_r$ is the absolute magnetic permeability of the magnetic material in which $\mu_0$ and $\mu_r$ are respectively the vacuum permeability and the relative permeability of the magnetic material (with $\mu_r = 1$ for the vacuum or $\mu_r \neq 1$ for the PMs/iron).

### B. Exact SD Technique

To distinguish between results influenced by relative permeability values of rotor core and stator teeth, it is important to assumed that Region VII and VIII have infinitely permeable. In this situation, these regions do not contribute to the system being solved. It is very easy to introduce these regions into HAM.

From (1), the general PDEs in terms of $\boldsymbol{A}$ in Region I ~ V can be written as

$$\nabla^2 \boldsymbol{A} = -\mu_o \nabla \times \boldsymbol{Mr} \quad \text{in Region I and IV} \tag{2a}$$

$$\nabla^2 \boldsymbol{A} = 0 \quad \text{in Region II and III} \tag{2b}$$

$$\nabla^2 \boldsymbol{A} = -\mu_0 \boldsymbol{J} \quad \text{in Region V} \tag{2c}$$

The field vectors $\boldsymbol{B} = \{B_r; B_\theta; 0\}$ and $\boldsymbol{H} = \{H_r; H_\theta; 0\}$ are coupled by

$$\boldsymbol{B} = \mu_m \boldsymbol{H} + \mu_o \boldsymbol{Mr} \quad \text{in Region I and IV} \tag{3a}$$

$$\boldsymbol{B} = \mu_0 \boldsymbol{H} \quad \text{in other regions} \tag{3b}$$

Using $\boldsymbol{B} = \nabla \times \boldsymbol{A}$, the components of $\boldsymbol{B}$ can be deduced by

$$B_r = \frac{1}{r}\frac{\partial A_z}{\partial \theta} \quad \text{and} \quad B_\theta = -\frac{\partial A_z}{\partial r} \tag{4}$$

To obtain the solution of magnetic field in different regions, the separation of variables method and the Dubas'

**DOI**: 10.1109/TMAG.2021.3127359, IEEE TRANSACTIONS ON MAGNETICS

superposition technique can be used to solve the PDEs. All regions of the proposed machine are described by Fourier series expression in both directions (i.e., $r$- and $\theta$-edges). Hence, the general solution of $A_z$, in subdomains is the superposition of two components in $r$- and $\theta$-directions [3].

In polar coordinates $(r, \theta)$, (2) in terms of $\boldsymbol{A} = \{0; 0; A_z\}$ can be rewritten as

- in Region I and IV (i.e., Poisson's equation):

$$\frac{\partial^2 A_z^{I,IV}}{\partial r^2} + \frac{1}{r}\frac{\partial A_z^{I,IV}}{\partial r} + \frac{1}{r^2}\frac{\partial^2 A_z^{I,IV}}{\partial \theta^2} = -\frac{\mu_0}{r}\left(Mr_\theta - \frac{\partial Mr_r}{\partial \theta}\right) \quad (5)$$

The general solution of $A_z$ is given as follows:

$$\begin{aligned} A_z^{I,IV} = & \sum_n \left(C_{3n}^{I,IV} r^{np} + C_{4n}^{I,IV} r^{-np} + \Upsilon_s\right) \sin(np\theta) \\ & + \sum_n \left(C_{5n}^{I,IV} r^{np} + C_{6n}^{I,IV} r^{-np} + \Upsilon_c\right) \cos(np\theta) \end{aligned} \quad (6)$$

where $\Upsilon_s$ and $\Upsilon_c$ are the particular solutions of (5).

- in Region II and III (i.e., Laplace's equation):

$$\frac{\partial^2 A_z^{II,III}}{\partial r^2} + \frac{1}{r}\frac{\partial A_z^{II,III}}{\partial r} + \frac{1}{r^2}\frac{\partial^2 A_z^{II,III}}{\partial \theta^2} = 0 \quad (7)$$

In these regions, the general solution of $A_z$ is:

$$\begin{aligned} A_z^{II,III} = & \sum_n \left(C_{3n}^{II,III} r^{np} + C_{4n}^{II,III} r^{-np}\right) \sin(np\theta) \\ & + \sum_n \left(C_{5n}^{II,III} r^{np} + C_{6n}^{II,III} r^{-np}\right) \cos(np\theta) \end{aligned} \quad (8)$$

- in Region V (i.e., Poisson's equation):

$$\frac{\partial^2 A_z^{V}}{\partial r^2} + \frac{1}{r}\frac{\partial A_z^{V}}{\partial r} + \frac{1}{r^2}\frac{\partial^2 A_z^{V}}{\partial \theta^2} = -\mu_0 J_z \quad (9)$$

in which

$$A_{zs}^V = \begin{array}{l} C_{s1}^V + C_{s2}^V \ln(r) - \frac{1}{4}\mu_0 J_{zs} r^2 \\ + \sum_m G_{sm}^\theta \cos\left[\beta_m\left(\theta - \alpha_s + \frac{w}{2}\right)\right] \\ + \sum_v G_{sv}^r \sin\left[\lambda_v \ln\left(\frac{r}{R_3}\right)\right] \end{array} \quad (10a)$$

$$\begin{cases} G_{sm}^\theta = C_{s3m}^V \left(\frac{r}{R_4}\right)^{\beta_m} + C_{s4m}^V \left(\frac{r}{R_3}\right)^{-\beta_m} \\ G_{sv}^r = \begin{array}{l} C_{s5v}^V \frac{\sinh\left[\lambda_v\left(\theta - \alpha_s + \frac{w}{2}\right)\right]}{\sinh(\lambda_v w)} \\ + C_{s6v}^V \frac{\sinh\left[\lambda_v\left(\theta - \alpha_s - \frac{w}{2}\right)\right]}{\sinh(\lambda_v w)} \end{array} \end{cases} \quad (10b)$$

with

$$J_{zs} = J_m[1 \ 1 \ 0 \ -1 \ -1 \ 0 \ 1 \ 1 \ 0 \ -1 \ -1 \ 0] \quad (11)$$

where $J_m$ is the current density peak, $\alpha_s$ is the position of $s^{th}$ coils with $s = 1, \cdots, Q$ in which $Q$ is the number of stator slots, $m$ and $v$ are the spatial harmonic orders, $\beta_m$ and $\lambda_v$ are the spatial frequency (or periodicity) in both directions defined by

$$\beta_m = \frac{m\pi}{w} \quad \& \quad \lambda_v = \frac{v\pi}{\ln(R_4/R_3)} \quad (12)$$

where $w$ is the slot-opening.

### C. 2-D FDM

The solution of the magnetic potential vector distribution in Region VI can be achieved by Maxwell's equations using numerical finite-difference approximations. In Fig. 2, the regular discretization of nodes is presented with each node connected to four neighboring nodes. From (1), the distribution of $A_z$ in Region VI can be expressed as:

$$\frac{\Delta^2 A_z^{VI}}{\Delta r^2} + \frac{1}{r}\frac{\Delta A_z^{VI}}{\Delta r} + \frac{1}{r^2}\frac{\Delta^2 A_z^{VI}}{\Delta \theta^2} = 0 \quad (13)$$

Based on (4), the distribution of $\boldsymbol{B}$ can be written as:

$$B_r = \lim_{\Delta\theta \to 0}\left(\frac{1}{r}\frac{\Delta A_z^{VI}}{\Delta \theta}\right) \ \& \ B_\theta = \lim_{\Delta r \to 0}\left(-\frac{\Delta A_z^{VI}}{\Delta r}\right) \quad (14a)$$

The difference quotient $B_r$ and $B_\theta$ is a derivative approximation. This improves as $\Delta$r and $\Delta\theta$ become smaller. $\Delta$r and $\Delta\theta$ are the spacing between two adjacent nodes in the $r$- and $\theta$-direction, respectively

$$\Delta\theta = \theta_{s,j+1} - \theta_{s,j} \quad (14b)$$

$$\Delta r = R_{3,i+1} - R_{3,i} \quad (14c)$$

According to (13) and Fig. 2, each term of the PDE at the particular node is replaced by a finite-difference approximation. The distribution of $A_z$ in Region VI can be rewritten as:

$$\begin{aligned} & \frac{A_{zs,i+1,j}^{VI} - 2A_{zs,i,j}^{VI} + A_{zs,i-1,j}^{VI}}{\Delta r^2} + \frac{1}{R_i}\frac{A_{zs,i+1,j}^{VI} - A_{zs,i-1,j}^{VI}}{2\Delta r} \\ & + \frac{1}{R_i^2}\frac{A_{zs,i,j+1}^{VI} - 2A_{zs,i,j}^{VI} + A_{zs,i,j-1}^{VI}}{\Delta\theta^2} = 0 \end{aligned} \quad (15)$$

This remains valid except for black nodes [see Fig. 2], however, for red and blue nodes, this equation must respect the distance between two adjacent nodes.

The Fourier's constants of (6), (8) and (10) must to be determined by applying boundary conditions (BCs). These BCs must satisfy the continuity of $\perp$ component of $\boldsymbol{B}$ (or the continuity of $\boldsymbol{A}$) and the continuity of the $\parallel$ component of $\boldsymbol{H}$. The detail equations set for these coefficients is given in Appendix B.

## IV. Comparison of HAM and Numerical Calculations

The model is tested on the machine given in Table I. In the middle of Region II (i.e., the inner air-gap), the magnetic flux density distribution for no-load, armature reaction current and on-load conditions are illustrated in Fig. 3, Fig. 4 and Fig. 5, respectively. In the middle of Region V and VI (i.e., the teeth and slots), the magnetic flux density distribution is illustrated in Fig. 6 and Fig. 7.

To give excellent results, finite number of spatial harmonics is supposed equal to 140. The 2-D FDM mesh should also have an appropriate node number to avoid time-cost, viz., $Nc = 25$ and $Nl = 25$. Highly accurate results are achieved between HAM approach and FEA whatever the relative permeability values of stator teeth.

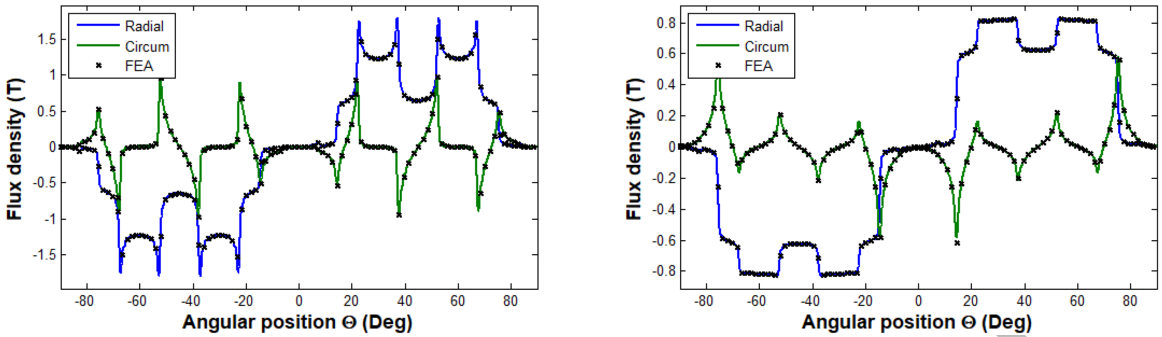


a) b)

Fig. 3. The $r$- and $\theta$-component of $\boldsymbol{B}$ in the middle of Region II at no-load condition calculated by HAM and verified by FEA for: (a) $\mu_r = 1{,}000$ and (b) $\mu_r = 2$.

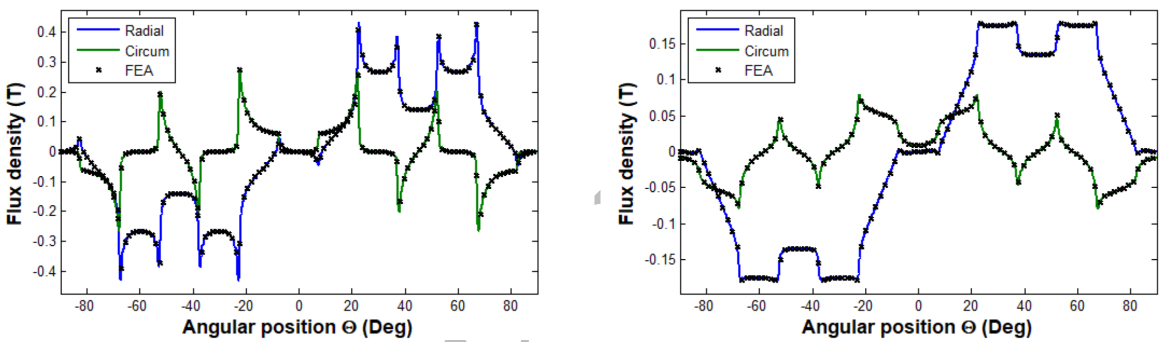


a) b)

Fig. 4. The $r$- and $\theta$-component of $\boldsymbol{B}$ in the middle of Region II under armature reaction current with a single-layer winding calculated by HAM and verified by FEA for: (a) $\mu_r = 1{,}000$ and (b) $\mu_r = 2$.

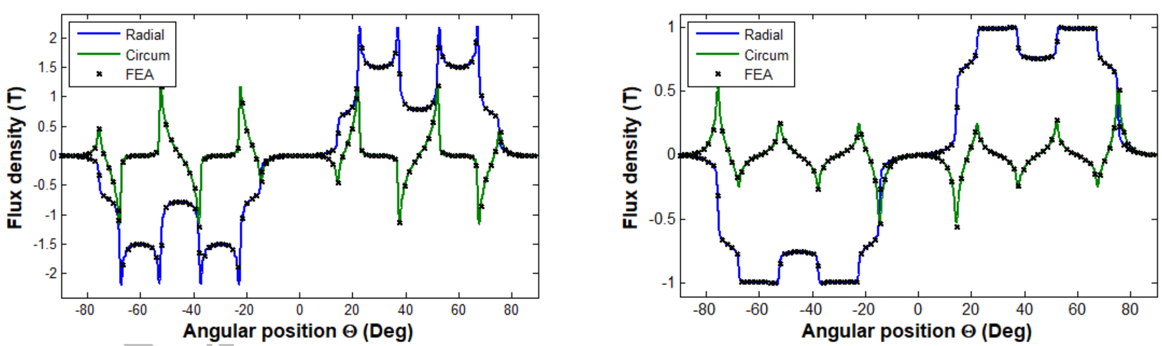


a) b)

Fig. 5. The $r$- and $\theta$-component of $\boldsymbol{B}$ in the middle of Region II at on-load condition calculated by HAM and verified by FEA for: (a) $\mu_r = 1{,}000$ and (b) $\mu_r = 2$.

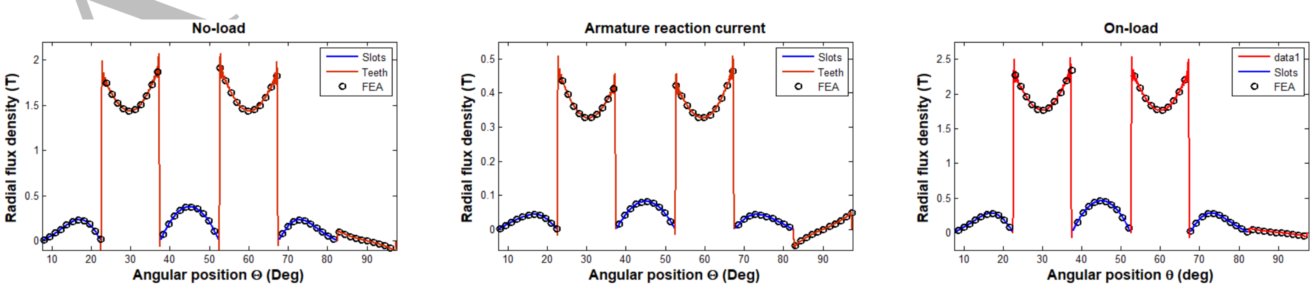

**DOI**: 10.1109/TMAG.2021.3127359, IEEE TRANSACTIONS ON MAGNETICS

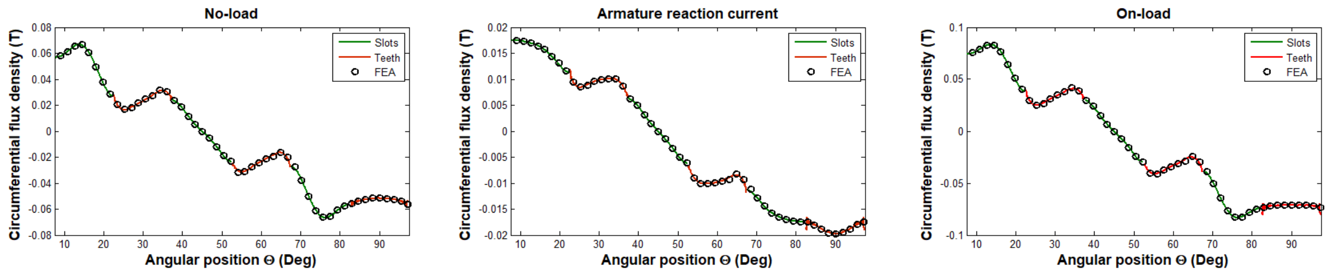


Fig. 6. The $r$- and $\theta$-component of $\boldsymbol{B}$ in the middle of slots and teeth calculated by HAM and verified by FEA for $\mu_r = 1{,}000$.

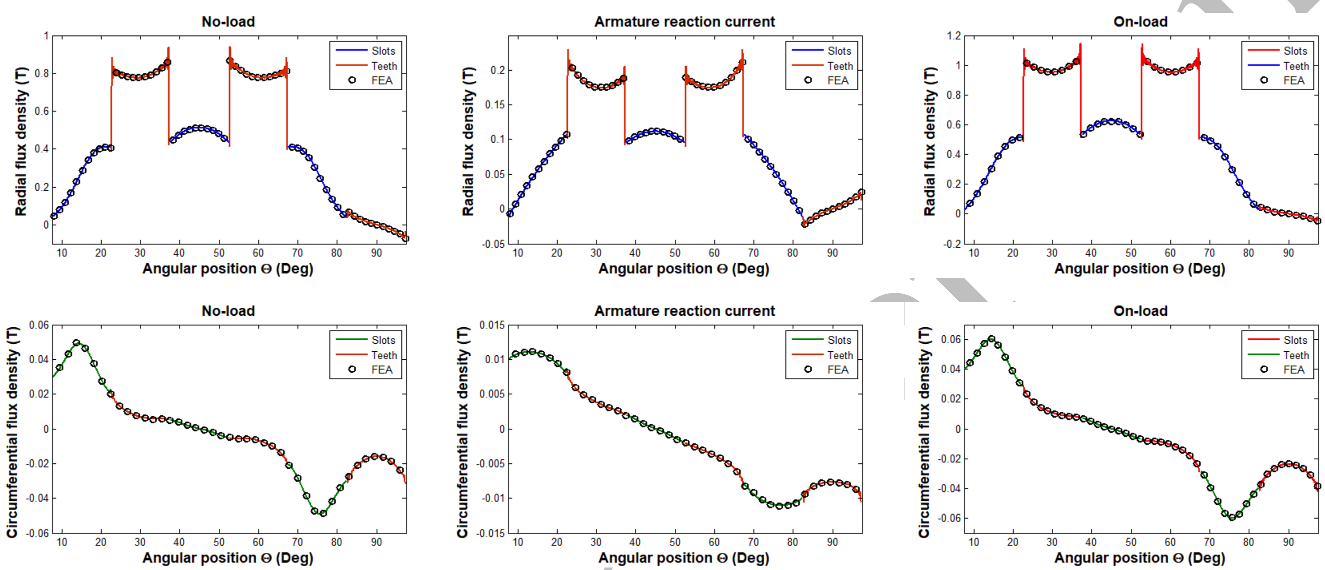


Fig. 7. The $r$- and $\theta$-component of $\boldsymbol{B}$ in the middle of slots and teeth calculated by HAM and verified by FEA for $\mu_r = 2$.

TABLE .1
MACHINE CHARACTERISTICS

| Symbol | Parameter (unit) | Value |
|---|---|---|
| $B_{rm}$ | Remanent flux density of PMs (T) | 1.25 |
| $p$ | Number of pole pairs | 2 |
| - | Magnetization type | Radial |
| $Q$ | Number of stator slots | 12 |
| $R_0$ | Inner radius (mm) | 30.00 |
| $R_1$ | Inner PM radius (mm) | 57.50 |
| $R_2$ | Outer PM radius (mm) | 64.00 |
| $R_3$ | Inner slot radius (mm) | 64.65 |
| $R_4$ | Outer slot radius (mm) | 79.65 |
| $R_5$ | Inner PM radius (mm) | 80.30 |
| $R_6$ | Outer PM radius (mm) | 86.80 |
| $R_7$ | Outer radius (mm) | 102.00 |
| $\beta$ | PM pole-arc to pole-pitch ratio | 61/90 |
| $w$ | Slot opening (deg) | 15.00 |
| $J_m$ | Armature current density (A/mm$^2$) | 10 |
| $L$ | Axial length (mm) | 150 |
| $N_s$ | Conductors per slot | 50 |
| $nh$ | Harmonics number in other regions | 140 |

## V. ELECTROMAGNETIC PERFORMANCES CALCULATION

### A. Cogging Torque

The cogging torque calculation in the proposed machine can be affected by the PM installed on the mobile core with the stator teeth. It is calculated from Maxwell stress method as:

$$C_t = \frac{LR^2}{\mu_0} \int_0^{2\pi} B_r^{II} B_\theta^{II} d\theta \tag{16}$$

where $L$ is the axial length of the machine, $R$ is the radius circle placed at the middle of Region II, and $B_r^{II}$ & $B_\theta^{II}$ are respectively the $r$- and $\theta$-component of $\boldsymbol{B}$ calculated under no-load condition in the middle of Region II.

### B. Flux Linkage and Back Electromotive Force (EMF)

Based on the Stokes' theorem, the flux linkage can be calculated from the distribution of $A_z$ in Region V as:

$$\varphi_s = \frac{LN_s}{S} \int_{\alpha_s - \frac{w}{2}}^{\alpha_s + \frac{w}{2}} \int_{R_3}^{R_4} A_{zs}^V \, r dr d\theta \tag{17}$$

where $S = w\left({R_4}^2 - {R_3}^2\right)/2$ is the area of stator slot, and $N_s$ is the conductors' number.

The phase flux vector is given by:

$$\begin{bmatrix} \psi_a \\ \psi_b \\ \psi_c \end{bmatrix} = C\left[\varphi_1 \; \varphi_2 \; \dots \; \varphi_Q\right]^T \tag{18}$$

where $C$ is the winding connection matrix of the $q$-phases

**DOI**: 10.1109/TMAG.2021.3127359, IEEE TRANSACTIONS ON MAGNETICS

current and the stator slots which can be expressed by

$$C = \begin{bmatrix} 1 & 0 & 0 & -1 & 0 & 0 & 1 & 0 & 0 & -1 & 0 & 0 \\ 0 & 0 & 1 & 0 & 0 & -1 & 0 & 0 & 1 & 0 & 0 & -1 \\ 0 & -1 & 0 & 0 & 1 & 0 & 0 & -1 & 0 & 0 & 1 & 0 \end{bmatrix} \quad (19)$$

The *3*-phases back EMF can be derived as:

$$\begin{bmatrix} E_a \\ E_b \\ E_c \end{bmatrix} = \Omega \frac{d}{d\theta} \begin{bmatrix} \psi_a \\ \psi_b \\ \psi_c \end{bmatrix} \quad (20)$$

where $\Omega$ is the rotor angular speed.

The total harmonic distortion can be calculated by:

$$THD = \frac{\sqrt{\sum_{n=2}^{20} h(n)^2}}{h(1)} \times 100\% \quad (21)$$

where $h(1)$ is the fundamental harmonic.

Fig. 8 shows the cogging torque waveform and its harmonics spectra calculated under two relative permeability values (viz., 2 and 1,000) for one period which is equal to 30°. The rotation step of the moving armature is assumed to be equal to 0.25°.

Fig. 9 and Fig. 10 show respectively the flux linkage per phase and back EMF waveform and its harmonics spectra calculated under two relative permeability values (viz., 2 and 1,000). The rotation step of the moving armature is proposed equal to 1°. For harmonics, the fundamental is assumed to be 1 per-unit (P.U) regardless of the cogging torque or back EMF. Excellent agreement between HAM and FEA.

Table II shown the computation time for the magnetic flux density and electromagnetic performances calculation by different methods such as HAM, SD technique and FEA. The 2-D HAM is ≈ 6 times faster than 2-D FEA with high accuracy.

TABLE II.
2-D COMPUTATIONAL TIME FOR VARIOUS METHODS

| **Method** | **HAM** | **SD technique** | **FEA** |
|---|---|---|---|
| | $nh = 140$<br>$Nc = 25, Nl = 25$ | $nh = 140$ | Whole machine<br>107,961 nodes |
| **Time (sec)** | ~4 | ~1.5 | ~25 |

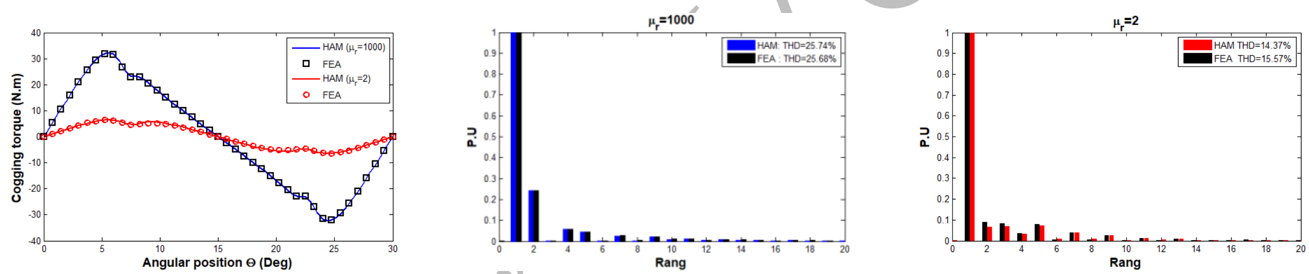


a) b)

Fig. 8. Cogging torque calculated by HAM and verified by FEA for $\mu_r = 1{,}000$ and $\mu_r = 2$: a) waveform, and b) harmonic spectrum.

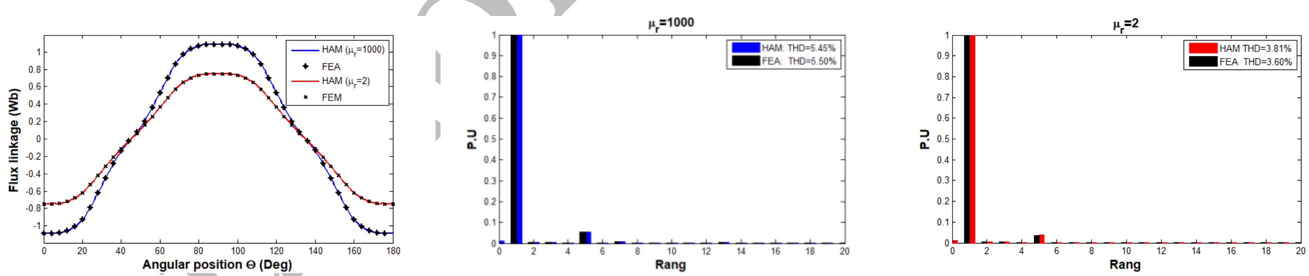


a) b)

Fig. 9. Flux linkage per phase calculated by HAM and verified by FEA for $\mu_r = 1{,}000$ and $\mu_r = 2$: a) waveform, and b) harmonic spectrum.

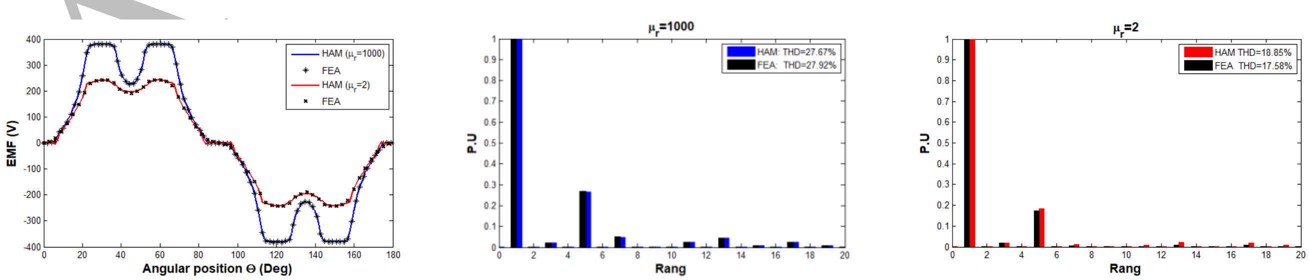


a) b)

Fig. 10. Back EMF per phase calculated by HAM and verified by FEA for $\mu_r = 1{,}000$ and $\mu_r = 2$: a) waveform, and b) harmonic spectrum.

**DOI**: 10.1109/TMAG.2021.3127359, IEEE TRANSACTIONS ON MAGNETICS

## VI. Conclusion

In this paper, a novel 2-D HAM in polar coordinates has been proposed for the dual-rotor PM synchronous machines having a radial magnetization and a single-layer concentrated winding. The developed approach is based on the exact SD technique and the FDM. These two models have been coupled in both directions (i.e., $r$- and $\theta$-edges) of the (non-)periodicity direction (i.e., in the interface between teeth regions and all its adjacent regions as slots and/or air-gap). The magnetic flux density distribution has been calculated in all regions under two relative permeability values of iron core whatever the load conditions. Moreover, the electromagnetic performances have been studied. Highly accurate results have been obtained between the proposed HAM and FEA. The computational time is ≈ 6 times smaller than 2-D FEA with high accuracy.

The high impact contributions of this approach can now focus our attention on the optimization of the machine performances, in particular with the local saturation effect through E-SD technique by inserting the *B(H)* curve which will be proposed in a future contribution.

## Appendix A

The remanent magnetization vector of PMs can be written as:

$$\boldsymbol{Mr} = Mr_r\,\boldsymbol{u_r} + Mr_\theta\,\boldsymbol{u_\theta} \tag{A1}$$

with

$$Mr_r = \sum_n Mr_{rsn}\sin(np\theta) + Mr_{rcn}\cos(np\theta) \tag{A2a}$$

$$Mr_\theta = \sum_n Mr_{\theta sn}\sin(np\theta) + Mr_{\theta cn}\cos(np\theta) \tag{A2b}$$

For a radial magnetization, we have

$$Mr_{rsn} = m_{rn}\frac{B_{rm}}{\mu_o}\sin\left(\frac{n\pi}{2}\right)\cos(np\tau) \tag{A3a}$$

$$Mr_{rcn} = m_{rn}\frac{B_{rm}}{\mu_o}\sin\left(\frac{n\pi}{2}\right)\sin(np\tau) \tag{A3b}$$

$$Mr_{\theta sn} = Mr_{\theta cn} = 0 \tag{A3c}$$

where $B_{rm}$ is the remanent flux density of PMs, $\tau$ is the angular position of PMs, and

$$m_{rn} = \frac{4}{\pi}\int_0^{\delta\pi/2}\cos(n\theta)d\theta \tag{A4}$$

with $\delta$ is the PM pole-arc to pole-pitch ratio.

## Appendix B

The BCs allow to determine the Fourier's constants of (6), (8) and (10).

On the $\theta$-direction:

- At $r = R_1$ and $\forall\theta$:

$$H_\theta^I(R_1,\theta) = 0 \tag{B1a}$$

which gives:

$$np\begin{pmatrix} C_{3n}^I R_1^{np-1} \\ -C_{4n}^I R_1^{-np-1}\end{pmatrix} = -\left.\frac{d\Gamma_s}{dr}\right|_{r=R_1} + \frac{1}{\mu_0}M_{\theta sn} \tag{B1b}$$

$$np\begin{pmatrix} C_{5n}^I R_1^{np-1} \\ -C_{6n}^I R_1^{-np-1}\end{pmatrix} = -\left.\frac{d\Gamma_c}{dr}\right|_{r=R_1} + \frac{1}{\mu_0}M_{\theta cn} \tag{B1c}$$

- At $r = R_2$ and $\forall\theta$:

$$A_z^I(R_2,\theta) = A_z^{II}(R_2,\theta) \tag{B2a}$$

which gives:

$$\begin{pmatrix} C_{3n}^I R_2^{np} \\ +C_{4n}^I R_2^{-np}\end{pmatrix} - \begin{pmatrix} C_{3n}^{II} R_2^{np} \\ +C_{4n}^{II} R_2^{-np}\end{pmatrix} = -\Gamma_s\big|_{r=R_2} \tag{B2b}$$

$$\begin{pmatrix} C_{5n}^I R_2^{np} \\ +C_{6n}^I R_2^{-np}\end{pmatrix} - \begin{pmatrix} C_{5n}^{II} R_2^{np} \\ +C_{6n}^{II} R_2^{-np}\end{pmatrix} = -\Gamma_c\big|_{r=R_2} \tag{B2c}$$

$$H_\theta^I(R_2,\theta) = H_\theta^{II}(R_2,\theta) \tag{B3a}$$

which gives:

$$np\left[\begin{pmatrix} C_{3n}^I R_2^{np-1} \\ -C_{4n}^I R_2^{-np-1}\end{pmatrix} - \begin{pmatrix} C_{3n}^{II} R_2^{np-1} \\ -C_{4n}^{II} R_2^{-np-1}\end{pmatrix}\right] = -\left.\frac{d\Gamma_s}{dr}\right|_{r=R_2} + \frac{1}{\mu_0}Mr_{\theta sn} \tag{B3b}$$

$$np\left[\begin{pmatrix} C_{5n}^I R_2^{np-1} \\ -C_{6n}^I R_2^{-np-1}\end{pmatrix} - \begin{pmatrix} C_{5n}^{II} R_2^{np-1} \\ -C_{6n}^{II} R_2^{-np-1}\end{pmatrix}\right] = -\left.\frac{d\Gamma_c}{dr}\right|_{r=R_2} + \frac{1}{\mu_0}Mr_{\theta cn} \tag{B3c}$$

- At $r = R_3$ and for the index $\mathrm{s} = 1,\cdots,Q$:

$$A_{zs,1,j}^{VI} = \frac{1}{\Delta\theta}\int_{\theta_{s,j}}^{\theta_{s,j+1}} A_z^{II}(R_3,\theta)d\theta \tag{B4}$$

$$\left(A_{zs}^V(R_3,\theta) = A_z^{II}(R_3,\theta)\right)\Big|^{\alpha_s - \frac{w}{2}\le\theta\le\alpha_s+\frac{w}{2}} \tag{B5a}$$

which gives:

$$C_{s1}^V + C_{s2}^V\ln(R_3) - \frac{1}{4}\mu_o J_{zs}R_3^2 = \frac{1}{w}\int_{\alpha_s-\frac{w}{2}}^{\alpha_s+\frac{w}{2}} A_z^{II}(R_3,\theta)\,d\theta \tag{B5b}$$

$$C_{s3m}^V\left(\frac{R_3}{R_4}\right)^{\beta_m} + C_{s4m}^V = \frac{2}{w}\int_{\alpha_s-\frac{w}{2}}^{\alpha_s+\frac{w}{2}} A_z^{II}(R_3,\theta)\cos\left[\beta_m\left(\theta-\alpha_s+\frac{w}{2}\right)\right]d\theta \tag{B5c}$$

$$H_\theta^{II}(R_3,\theta) = \sum_s\begin{pmatrix} H_{\theta s}^V(R_3,\theta)\Big|^{\alpha_s-\frac{w}{2}\le\theta\le\alpha_s+\frac{w}{2}} \\ +H_{\theta s}^{VI}(R_3,\theta)\Big|^{\alpha_s+\frac{w}{2}\le\theta\le\alpha_{s+1}-\frac{w}{2}}\end{pmatrix} \tag{B6a}$$

In order to satisfy (B6a), the magnetic flux intensity $H^{VI}_{\theta s}(R_3,\theta)$ by applying (14a) should be written as:

$$H^{VI}_{\theta s}(R_3,\theta) = -\frac{1}{\mu_0\mu_r}\sum_{j=2}^{Nc-1}\left(\frac{A^{VI}_{s,2,j}-A^{VI}_{s,1,j}}{\Delta r}\right) f_v \quad \text{(B6b)}$$

$$f_v = \sum_{v}\left[h^{VI}_{\theta sv}\sin(vp\theta) + h^{VI}_{\theta cv}\cos(vp\theta)\right] \quad \text{(B6c)}$$

where $h^{VI}_{\theta sv}$ & $h^{VI}_{\theta cv}$ are the Fourier's constants, and $Nc$ is the number of grid nodes in the $\theta$-direction.

Development of (B6a) gives:

$$\begin{aligned} -\mu_0 np\left(C^{II}_{3n}R_3^{np-1} - C^{II}_{4n}R_3^{-np-1}\right) = \\ \frac{1}{\pi}\sum_{s=1}^{Q}\int_{\alpha_s-\frac{w}{2}}^{\alpha_s+\frac{w}{2}} H^{V}_{\theta s}(R_3,\theta)\sin(np\theta)\,d\theta \\ +\frac{1}{\pi}\sum_{s=1}^{Q}\int_{\alpha_s+\frac{w}{2}}^{\alpha_{s+1}-\frac{w}{2}} H^{VI}_{\theta s}(R_3,\theta)\sin(np\theta)\,d\theta \end{aligned} \quad \text{(B6d)}$$

$$\begin{aligned} -\mu_0 np\left(C^{II}_{5n}R_3^{np-1} - C^{II}_{6n}R_3^{-np-1}\right) = \\ \frac{1}{\pi}\sum_{s=1}^{Q}\int_{\alpha_s-\frac{w}{2}}^{\alpha_s+\frac{w}{2}} H^{V}_{\theta s}(R_3,\theta)\cos(np\theta)\,d\theta \\ +\frac{1}{\pi}\sum_{s=1}^{Q}\int_{\alpha_s+\frac{w}{2}}^{\alpha_{s+1}-\frac{w}{2}} H^{VI}_{\theta s}(R_3,\theta)\cos(np\theta)\,d\theta \end{aligned} \quad \text{(B6e)}$$

where the Fourier's constants of (B6c) can be written as:

$$\begin{cases} h^{VI}_{\theta sv} = \dfrac{2p}{\pi}\displaystyle\int_{\theta_{s,j}}^{\theta_{s,j+1}} \sin(vp\theta)\,d\theta & \text{(B6f)} \\ h^{VI}_{\theta cv} = \dfrac{2p}{\pi}\displaystyle\int_{\theta_{s,j}}^{\theta_{s,j+1}} \cos(vp\theta)\,d\theta & \text{(B6g)} \end{cases}$$

- At $r = R_4$ and for the index $s = 1, \cdots, Q$:

$$A^{VI}_{zs,NL,j} = \frac{1}{\Delta\theta}\int_{\theta_{s,j}}^{\theta_{s,j+1}} A^{III}_z(R_4,\theta)d\theta \quad \text{(B7)}$$

$$\left(A^{V}_{zs}(R_4,\theta) = A^{III}_z(R_4,\theta)\right)\Big|^{\alpha_s-\frac{w}{2}\le\theta\le\alpha_s+\frac{w}{2}} \quad \text{(B8a)}$$

which gives:

$$C^{V}_{s1} + C^{V}_{s2}\ln(R_4) - \frac{1}{4}\mu_o J_{zs}R_4^2 = \frac{1}{w}\int_{\alpha_s-\frac{w}{2}}^{\alpha_s+\frac{w}{2}} A^{III}_z(R_3,\theta)\,d\theta \quad \text{(B8b)}$$

$$C^{V}_{x3m} + C^{V}_{x4m}\left(\frac{R_4}{R_3}\right)^{-\beta_m} = \frac{2}{w}\int_{\alpha_s-\frac{w}{2}}^{\alpha_s+\frac{w}{2}} A^{III}_z(R_3,\theta)\cos\left[\beta_m\left(\theta-\alpha_s+\frac{w}{2}\right)\right]d\theta \quad \text{(B8c)}$$

$$H^{III}_{\theta}(R_4,\theta) = \sum_{s}\begin{pmatrix} H^{V}_{\theta s}(R_4,\theta)\Big|^{\alpha_s-\frac{w}{2}\le\theta\le\alpha_s+\frac{w}{2}} \\ +H^{VI}_{\theta s}(R_4,\theta)\Big|^{\alpha_s+\frac{w}{2}\le\theta\le\alpha_{s+1}-\frac{w}{2}} \end{pmatrix} \quad \text{(B9a)}$$

In order to satisfy (B9a), the magnetic flux intensity $H^{VI}_{\theta s}(R_4,\theta)$ by applying (14a) should be written as:

$$H^{VI}_{\theta s}(R_4,\theta) = -\frac{1}{\mu_0\mu_r}\sum_{j=2}^{Nc-1}\left(\frac{A^{VI}_{s,Nl,j}-A^{VI}_{s,Nl-1,j}}{\Delta r}\right) f_v \quad \text{(B9b)}$$

Development of (B9a) gives:

$$\begin{aligned} -\mu_0 np\left(C^{III}_{3n}R_4^{np-1} - C^{III}_{4n}R_4^{-np-1}\right) = \\ \frac{1}{\pi}\sum_{s=1}^{Q}\int_{\alpha_s-\frac{w}{2}}^{\alpha_s+\frac{w}{2}} H^{V}_{\theta s}(R_4,\theta)\sin(np\theta)\,d\theta \\ +\frac{1}{\pi}\sum_{s=1}^{Q}\int_{\alpha_s+\frac{w}{2}}^{\alpha_{s+1}-\frac{w}{2}} H^{VI}_{\theta s}(R_4,\theta)\sin(np\theta)\,d\theta \end{aligned} \quad \text{(B9c)}$$

$$\begin{aligned} -\mu_0 np\left(C^{III}_{5n}R_4^{np-1} - C^{III}_{6n}R_4^{-np-1}\right) = \\ \frac{1}{\pi}\sum_{s=1}^{Q}\int_{\alpha_s-\frac{w}{2}}^{\alpha_s+\frac{w}{2}} H^{V}_{\theta s}(R_4,\theta)\cos(np\theta)\,d\theta \\ +\frac{1}{\pi}\sum_{s=1}^{Q}\int_{\alpha_s+\frac{w}{2}}^{\alpha_{s+1}-\frac{w}{2}} H^{VI}_{\theta s}(R_4,\theta)\cos(np\theta)\,d\theta \end{aligned} \quad \text{(B9d)}$$

- At $r = R_5$ and $\forall\theta$:

$$A^{III}_z(R_5,\theta) = A^{IV}_z(R_5,\theta) \quad \text{(B10a)}$$

which gives:

$$\begin{pmatrix} C^{IV}_{3n}R_5^{np} \\ +C^{IV}_{4n}R_5^{-np} \end{pmatrix} - \begin{pmatrix} C^{III}_{3n}R_5^{np} \\ +C^{III}_{4n}R_5^{-np} \end{pmatrix} = -\Gamma_s|_{r=R_5} \quad \text{(B10b)}$$

$$\begin{pmatrix} C^{IV}_{5n}R_5^{np} \\ +C^{IV}_{6n}R_5^{-np} \end{pmatrix} - \begin{pmatrix} C^{III}_{5n}R_5^{np} \\ +C^{III}_{6n}R_5^{-np} \end{pmatrix} = -\Gamma_c|_{r=R_5} \quad \text{(B10c)}$$

$$H^{III}_{\theta}(R_5,\theta) = H^{IV}_{\theta}(R_5,\theta) \quad \text{(B11a)}$$

which gives:

$$np\left[\begin{pmatrix} C^{IV}_{3n}R_5^{np-1} \\ -C^{IV}_{4n}R_5^{-np-1} \end{pmatrix} - \begin{pmatrix} C^{III}_{3n}R_5^{np-1} \\ -C^{III}_{4n}R_5^{-np-1} \end{pmatrix}\right] = -\frac{d\Gamma_s}{dr}\bigg|_{r=R_5} + \frac{1}{\mu_0}Mr_{\theta sn} \quad \text{(B11b)}$$

$$np\left[\begin{pmatrix} C^{IV}_{5n}R_5^{np-1} \\ -C^{IV}_{6n}R_5^{-np-1} \end{pmatrix} - \begin{pmatrix} C^{III}_{5n}R_5^{np-1} \\ -C^{III}_{6n}R_5^{-np-1} \end{pmatrix}\right] =$$

$$-\frac{d\Gamma_c}{dr}\bigg|_{r=R_5} + \frac{1}{\mu_0} Mr_{\theta cn} \quad \text{(B11c)}$$

- At $r = R_6$ and $\forall\theta$:

$$H_\theta^{IV}(R_6,\theta) = 0 \quad \text{(B12a)}$$

which gives:

$$np\left(C_{3n}^{IV} R_6^{np-1} - C_{4n}^{IV} R_6^{-np-1}\right) = -\frac{d\Gamma_s}{dr}\bigg|_{r=R_6} + \frac{1}{\mu_0} Mr_{\theta sn} \quad \text{(B12b)}$$

$$np\left(C_{5n}^{IV} R_6^{np-1} - C_{6n}^{IV} R_6^{-np-1}\right) = -\frac{d\Gamma_c}{dr}\bigg|_{r=R_6} + \frac{1}{\mu_0} Mr_{\theta cn} \quad \text{(B12c)}$$

On the $r$-direction, viz., on the edges of the Region V and VI and for the index $s = 1, \cdots, Q$:

- for $\theta = \alpha_s + w/2$:

$$A_{zs,i,1}^{VI} = \frac{1}{\Delta r}\int_{R_{3,i}}^{R_{3,i+1}} A_{zs}^{V}\left(r, \alpha_s + \frac{w}{2}\right) dr \quad \text{(B13)}$$

$$H_{rs}^{VI}\left(r, \alpha_s + \frac{w}{2}\right) = H_{rs}^{V}\left(r, \alpha_s + \frac{w}{2}\right) \quad \text{(B14a)}$$

where

$$H_{rs}^{VI}\left(r, \alpha_s + \frac{w}{2}\right) = \frac{1}{\mu_r \mu_0}\sum_{i=2}^{Nl-1}\sum_{v}\left(\frac{1}{R_{3,i}}\frac{A_{zs,i,2}^{VI} - A_{zs,i,1}^{VI}}{\Delta\theta}\right) \cdot h_{rsv}^{VI} \sin\left[\lambda_v \ln\left(\frac{r}{R_3}\right)\right] \quad \text{(B14b)}$$

where $Nl$ is the number of grid nodes in the $r$-direction.

From (B14a) and (B14b), we have:

$$\lambda_v\left(C_{s5v}^{V}\cosh(\lambda_v w) + C_{s6v}^{V}\right) = \frac{1}{\mu_r}\sum_{i=2}^{Nl-1}\left(\frac{A_{s,i,2}^{VI} - A_{s,i,1}^{VI}}{\Delta\theta}\right) h_{rsv}^{VI} \quad \text{(B14c)}$$

where

$$h_{rsv}^{VI} = \frac{2}{\ln\left(\frac{R_4}{R_3}\right)}\int_{R_{3,i}}^{R_{3,i+1}} \frac{1}{r}\sin\left[\lambda_v \ln\left(\frac{r}{R_3}\right)\right] dr \quad \text{(B14d)}$$

- for $\theta = \alpha_s - w/2$:

$$A_{zs,i,Nc}^{VI} = \frac{1}{\Delta r}\int_{R_{3,i}}^{R_{3,i+1}} A_{z(s-1)}^{V}\left(r, \alpha_s - \frac{w}{2}\right) dr \quad \text{(B15)}$$

$$H_{rs}^{VI}\left(r, \alpha_s - \frac{w}{2}\right) = H_{r(s-1)}^{V}\left(r, \alpha_s - \frac{w}{2}\right) \quad \text{(B16a)}$$

where

$$H_{rs}^{VI}\left(r, \alpha_s - \frac{w}{2}\right) = \frac{1}{\mu_r \mu_0}\sum_{i=2}^{Nl-1}\sum_{v}\left(\frac{1}{R_{3,i}}\frac{A_{zs,i,Nc}^{VI} - A_{zs,i,Nc-1}^{VI}}{\Delta\theta}\right) \cdot h_{rsv}^{VI} \sin\left[\lambda_v \ln\left(\frac{r}{R_3}\right)\right] \quad \text{(B16b)}$$

From (B16a) and (B16b), we have:

$$\lambda_v\left(C_{s6v}^{V}\cosh(\lambda_v w) + C_{s5v}^{V}\right) = \frac{1}{\mu_r}\sum_{i=2}^{Nl-1}\left(\frac{A_{s,i,Nc}^{VI} - A_{s,i,Nc-1}^{VI}}{\Delta r}\right) h_{rsv}^{VI} \quad \text{(B16c)}$$

For the sake of simplification, the proposed machine is modeled for one half of the period. In this case, the anti-periodic BCs are:

$$A_{zQs,i,Nc}^{VI} = -\frac{1}{\Delta r}\int_{R_{3,i}}^{R_{3,i+1}} A_{z1}^{V}\left(r, \alpha_1 - \frac{w}{2}\right) dr \quad \text{(B17)}$$

$$H_{rQs}^{VI}\left(r, \alpha_1 - \frac{w}{2}\right) = -H_{r1}^{V}\left(r, \alpha_1 - \frac{w}{2}\right) \quad \text{(B18)}$$

## References


[1] F. Dubas, and C. Espanet, "Analytical solution of the magnetic field in permanent-magnet motors taking into account slotting effect: No-load vector potential and flux density calculation," *IEEE Trans. Magn.*, vol. 45, no. 5, pp. 2097-2109, May 2009, doi: 10.1109/TMAG.2009.2013245.

[2] F. Dubas, and K. Boughrara, "New scientific contribution on the 2-D subdomain technique in Cartesian coordinates: Taking into account of iron parts," *Math. Comput. Appl.*, vol. 22, no. 1, p. 17, Feb. 2017, doi: 10.3390/mca22010017.

[3] F. Dubas, and K. Boughrara, "New scientific contribution on the 2-D subdomain technique in polar coordinates: Taking into account of iron parts," *Math. Comput. Appl.*, vol. 22, no. 4, p. 42, Oct. 2017, doi: 10.3390/mca22040042.

[4] L. Roubache, K. Boughrara, F. Dubas and R. Ibtiouen, "New subdomain technique for electromagnetic performances calculation in radial-flux electrical machines considering finite soft-magnetic material permeability," *IEEE Trans. Magn*, vol. 54, no. 4, Apr. 2018, Art. no. 8103315, doi: 10.1109/TMAG.2017.2785254.

[5] L. Roubache, K. Boughrara, F. Dubas, and R. Ibtiouen, "Elementary subdomain technique for magnetic field calculation in rotating electrical machines with local saturation effect," *COMPEL - Int. J. Comput. Math. Electr. Electron. Eng.*, vol. 38, no. 1, pp. 24-45, Jan. 2019, doi: 10.1108/COMPEL-11-2017-0481.

[6] L. Roubache, K. Boughrara, F. Dubas, and R. Ibtinouen, "Technique en sous-domaines élémentaires dans les machines asynchrones à cage d'écureuil : Saturation magnétique locale & Courants de Foucault dans les barres," in *Proc. Symposium de Génie Électrique*, Nancy, France, 3-5 Jul. 2018.

[7] B.K. Kushwaha, G. Rituraj, and P. Kumar, "A subdomain analytical model of coil system with magnetic shields of finite dimensions and finite permeability for wireless power transfer systems," *IEEE Trans. Magn*, vol. 56, no. 12, Nov. 2020, Art. no. 8400511, doi: 10.1109/TMAG.2020.3028992.

[8] H. Zhang, M. Yang, Y. Zhang, J. Tuo, S. Luo, J. Xu, "Analytical field model of segmented Halbach array permanent magnet machines considering iron nonlinearity", *IET Elect. Power Appl.*, Early View, Jan. 2021, doi: 10.1049/elp2.12069

[9] B. Ladghem-Chikouche, and R. Ibtiouen, "Analytical approach for spoke-type permanent magnet machine including finite permeability of iron core", *COMPEL - Int. J. Comput. Math. Electr. Electron. Eng.*, Vol. 39 No. 2, pp. 333-352, Jan. 2020, doi: 10.1108/COMPEL-04-2019-0143.

[10] R.L.J. Sprangers, J.J.H. Paulides, B.L.J. Gysen, and E.A. Lomonova, "Magnetic saturation in semi-analytical harmonic modeling for electric machine analysis," *IEEE Trans. Magn.*, vol. 52, no. 2, Feb. 2016, Art. no. 8100410, doi: 10.1109/TMAG.2015.2480708.

[11] R.L.J. Sprangers, J.J.H. Paulides, B.L.J. Gysen, J. Waarma, and E.A. Lomonova, "Semianalytical framework for synchronous reluctance motor analysis including finite soft-magnetic material permeability," *IEEE Trans. Magn.*, vol. 51, no. 11, Nov. 2015, Art. no. 8110504, doi: 10.1109/TMAG.2015.2442419.

[12] Z. Djelloul-Khedda, K. Boughrara, F. Dubas, A. Kechroud, and B. Souleyman, "Semi-analytical magnetic field predicting in many structures of permanent-magnet synchronous machines considering the iron permeability," *IEEE Trans. Magn*, vol. 54, no. 7, July 2018, Art. no. 8103921, doi: 10.1109/TMAG.2018.282428.

[13] Z. Djelloul-Khedda, K. Boughrara, F. Dubas, and R. Ibtiouen, "Nonlinear analytical prediction of magnetic field and electromagnetic performances in switched reluctance machines," *IEEE Trans. Magn.*, vol. 53, no. 7, July 2017, Art. no. 8107311, doi: 10.1109/TMAG.2017.2679686.

[14] B. Ladghem-Chikouche, K. Boughrara, F. Dubas, and R. Ibtiouen, "2-D semi-analytical magnetic field calculation for flat permanent-magnet linear machines using exact subdomain technique," *IEEE Trans. Magn.*, vol. 57, no. 6, June 2021, Art. no. 8106211, doi: 10.1109/TMAG.2021.3068326.

[15] A. Rahideh, A. A. Vahaj, M. Mardaneh1, T. Lubin, "Two-dimensional analytical investigation of the parameters and the effects of magnetization patterns on the performance of coaxial magnetic gears," *IET Electr. Syst. Transp.*, vol. 7, no. 3, pp. 230-245, July 2017, doi: 10.1049/iet-est.2016.0070.

[16] K. Boughrara, B. Ladghem-Chikouche, R. Ibtiouen, D. Zarko, and Omar Touhami, "Analytical model of slotted air-gap surface mounted permanent-magnet synchronous motor with magnet bars magnetized in the shifting direction," *IEEE Trans. Magn.*, vol. 45, no. 2, pp. 747-758, Feb. 2009, doi**:** 10.1109/TMAG.2008.2008751.

[17] K. Abbaszadeh, and F. Rezaee Alam, "On-load field component separation in surface-mounted permanent-magnet motors using an improved conformal mapping method," *IEEE Trans. Magn.*, vol. 45, no. 2, Art. no. 5200112, Feb. 2016, doi**:** 10.1109/TMAG.2015.2493150.

[18] R. Behrooz and R. Farhad, "An improved conformal mapping method for magnetic field analysis in surface mounted permanent magnet motors," *COMPEL - Int. J. Comput. Math. Electr. Electron. Eng*., vol. 36, no. 4, pp. 892-905, July 2017, doi: 10.1108/COMPEL-07-2016-0284.

[19] A. Hanic, D. Zarko, D. Kuhinek, and Z. Hanic "On-load analysis of saturated surface permanent magnet machines using conformal mapping and magnetic equivalent circuits," *IEEE Trans. Magn*, vol. 33, no. 3, Sep. 2018, pp. 915-924, doi**:** 10.1109/TEC.2017.2789322.

[20] A. Hanic, D. Zarko, and Z. Hanic, "A novel method for no-load magnetic field analysis of saturated surface permanent-magnet machines using conformal mapping and magnetic equivalent circuits," *IEEE Trans. Magn*, vol. 31, no. 2, Nov. 2016, pp. 740-749, doi: 10.1109/TEC.2015.2507704.

[21] L.J. Wu, Z. Li, X. Huang, Y. Zhong, Y. Fang, and Z. Q. Zhu, "A hybrid field model for open-circuit field prediction in surface-mounted PM machines considering saturation," *IEEE Trans. Magn*, vol. 54, no. 6, June 2018, Art. no. 8103812, doi: 10.1109/TMAG.2018.2817178.

[22] Y. Liu, Z. Zhang, W. Geng, and J. Li, "A simplified finite-element model of hybrid excitation synchronous machines with radial/axial flux paths via magnetic equivalent circuit," *IEEE Trans. Magn*, vol. 53, no. 11, Nov. 2017, Art. no. 7403004, doi: 10.1109/TMAG.2017.2696568.

[23] B. Nedjar, L. Vido, S. Hlioui, Y. Amara, and M. Gabsi, "Hybrid coupling: magnetic equivalent circuit coupled to finite element analysis for PMSM electromagnetic modeling," *in Proc.* ISIE, pp. 858-862, Hangzhou, China, 28-31 May 2012, doi: 10.1109/ISIE.2012.6237201.

[24] K. Lee, M.J. DeBortoli, M.J. Lee, S.J. Salon, "Coupling Finite Elements and Analytical Solution in the Airgap of Electrical Machines," *IEEE Trans. Magn*., vol. 27, no. 5, Sep. 1991, pp. 3955-3957, doi: 10.1109/20.104969.

[25] M. Shen, P-D. Pfister, C. Tang, and Y. Fang, "A hybrid model permanent-magnet machines combining Fourier analytical model with finite element method, taking magnetic saturation into account," *IEEE Trans. Magn*, vol. 57, no. 2, Feb. 2021, doi: 10.1109/TMAG.2020.3005802.

[26] L. Wu, H. Yin, D. Wang, and Y. Fang, "On-load field prediction in SPM machines by a subdomain and magnetic circuit hybrid model," *IEEE Trans Ind. Elec.*, vol. 67, no. 9, pp. 7190-7201, Sep. 2020, doi: 10.1109/TIE.2019.2942561.

[27] H.S. Zhang, Z.X. Deng, M.L. Yang, Y. Zhang, J.Y. Tuo, and J. Xu, "Analytical prediction of Halbach array permanent magnet machines considering finite tooth permeability," *IEEE Trans. Magn.*, vol. 56, no. 6, June 2020, Art. no. 8101010, doi: 10.1109/TMAG.2020.2982844.

[28] S. Ouagued, Y. Amara, and G. Barakat, "Comparison of hybrid analytical modelling and reluctance network modelling for pre-design purposes," *Mathematics and Computers in Simulation*, vol. 130, pp. 3-21, Dec. 2016, doi: 10.1016/j.matcom.2016.05.001.

[29] S. Ouagued, Y. Amara, and G. Barakat, "Cogging force analysis of linear permanent magnet machines using a hybrid analytical model," *IEEE Trans. Magn*, vol. 52, no. 7, July 2016, Art. no. 8202704, doi: 10.1109/TMAG.2016.2521825.

[30] Y. Benmessaoud, F. Dubas, and M. Hilairet, "Combining the magnetic equivalent circuit and Maxwell-Fourier method for eddy-current loss calculation," *Math. Comput. Appl.*, vol. 24, no. 2, p. 60, June 2019, doi: 10.3390/mca24020060.

[31] Y. Benmessaoud, D. Ouamara, F. Dubas, and M. Hilairet, "Investigation of volumic permanent-magnet eddy-current losses in multi-phase synchronous machines from hybrid multi-layer model," *Math. Comput. Appl.*, vol. 25, no. 1, p. 14, Mar. 2020, doi: 10.3390/mca25010014.

[32] D. Ceylan, L.A. J. Friedrich, K.O. Boynov, and E.A. Lomonova, "Convergence analysis of the fixed-point method with the hybrid analytical modeling for 2-D nonlinear magnetostatic problems," *IEEE Trans. Magn*, Jan. 2021, Art. no. 7500105, doi**:** 10.1109/TMAG.2020.3024539.

[33] J. Bao, B.L.J. Gysen, and E.A. Lomonova, "Hybrid analytical modeling of saturated linear and rotary electrical machines: Integration of Fourier modeling and magnetic equivalent circuits," *IEEE Trans. Magn*, vol. 54, no. 11, Nov. 2018, Art. no. 8109905, doi: 10.1109/TMAG.2018.2837896.

[34] R. Benlamine, F. Dubas, S-A. Randi, D. Lhotellier, and C. Espanet, "3-D numerical hybrid method for PM eddy-current losses calculation: Application to axial-flux PMSMs," *IEEE Trans. Magn.*, vol. 51, no. 7, July 2015, Art. no. 8106110, doi: 10.1109/TMAG.2015.2405053.

[35] A. Demenko, J. K. Sykulski, "Analogies between Finite Difference and Finite Element Methods for Scalar and Vector Potential Formulations in Magnetic Field Calculations," *IEEE Trans. Magn*, vol. 52, no. 6, June 2016, Art. no. 7004206, doi**:** 10.1109/TMAG.2016.2521345.

[36] Q. Sun, R. Zhang, Q. Zhan, and Q. H. Liu, "3-D implicit–explicit hybrid finite difference/spectral element/finite element time domain method without a buffer zone," *IEEE Trans. Antennas Propag*., vol. 67, no. 8, Aug. 2019, pp. 5469-5476, doi: 10.1109/TAP.2019.2913740.

[37] Q. Sun, Q. Ren, Q. Zhan, and Q. H. Liu, "3-D domain decomposition based hybrid finite-difference time-domain/finite-element time-domain method with nonconformal meshes," *IEEE Trans. Microw. Theory Tech.*, vol. 65, no. 10, Oct. 2017, pp. 3682-3688, doi**:** 10.1109/TMTT.2017.2686386.

[38] B. Yan, Y. Yang X. Wang, "A semi-numerical method to assess start and synchronization performance of a line-start permanent magnet synchronous motor equipped with hybrid rotor," *IET Elect. Power Appl.*, vol. 15, no. 4, pp. 487-500, Feb. 2021, doi: 10.1049/elp2.12043.

[39] T. Carpi, Y. Lefèvre, and C. Henaux, "Hybrid modeling method of magnetic field of axial flux permanent magnet machine", XIII International Conference on Electrical Machines (ICEM), Greece. pp.766-772, Sep. 2018, doi: 10.1109/ICELMACH.2018.8506756

[40] K. Ramakrishnan, M. Curti, D. Zarko, G. Mastinu, J.J.H. Paulides, and E.A. Lomonova, "Comparative analysis of various methods for modelling surface permanent magnet machines," *IET Elect. Power Appl.*, vol. 11, no. 4, pp. 540-547, Apr. 2017, doi: 10.1049/iet-epa.2016.0720.

[41] L.J. Wu, Z.Q. Zhu, D.A. Staton, M. Popescu, and D. Hawkins, "Comparison of analytical models of cogging torque in surface-mounted PM machines," *IEEE Trans. Magn*, vol. 59, no. 6, June 2012, pp. 2414-2425, doi**:** 10.1109/TIE.2011.2143379.

[42] D.C. Meeker, "Finite Element Method Magnetics", Version 4.2, 2019, Build, http://www.femm.info.